Materials Advances

ROYAL SOCIETY OF CHEMISTRY

COMMUNICATION

View Article Online
View Journal | View Issue

Cite this: *Mater. Adv.*, 2023, 4, 1900

Received 7th December 2022,
Accepted 11th March 2023

DOI: 10.1039/d2ma01070d

rsc.li/materials-advances

Green one-pot synthesis of bimetallic Pd–Pt nanosponges using biomolecules with enhanced catalytic activity for hydrogen evolution reactions†

Fuat Topuz, *[ab] Bhushan Patil[a] and Tamer Uyar *[ac]

Green one-pot synthesis of bimetallic nanoparticles of Pd and Pt using RNA molecules as the capping/stabilizing agent and ascorbic acid as the reducing agent was described. Bimetallic nanoparticles have been used for hydrogen evolution reactions, which demonstrated improved catalytic performance than pure Pd nanoparticles and Pd/C materials.

Powered by nature, generating energy from sustainable sources has gained popularity to replace fossil energy sources. In this regard, using water as an energy source has become a useful technique to provide high-purity hydrogen through the decomposition of water into hydrogen and oxygen. This is a very energy-intensive process, and hence catalysts are used to reduce the required potential.[1] Noble metal nanocatalysts used for hydrogen evolution reactions (HER) showed high catalytic activity, the performance of which could be further increased by the use of bimetallic nanoparticles.[2]

HER electrocatalysts made from critical raw materials (CRM) such as platinum (Pt) and palladium (Pd) are the most efficient electrocatalysts; however, their high cost and limited geographic distribution increase the risk of a supply shortage.[1] Small electrocatalysts with high mass activity (MA) are in demand for fabricating lightweight small energy conversion and storage devices. Surface poisoning and poor stability are the two major challenges that must be overcome by the strong binding of Pt supported by preferred (111) facets. Therefore, the use of bimetallic particles with electrocatalytic reinforcement shows a very high catalytic performance compared to monometallic particles: the presence of a second metal effectively influences the electrocatalytic activity through the synergistic effect, and spillover of the HER intermediates avoiding Pt surface poisoning and leaving behind a clean Pt surface for the HER.[3]

Bimetallic nanoparticles with different morphologies and sizes have been synthesized using the combination of two different metallic components.[4] In this regard, various reducing, stabilizing and binding agents have been employed for the production of shape-controlled noble metal catalysts, including green reagents such as biomass,[5] plant extracts,[6] and RNA,[7,8] which were used for the synthesis of highly branched Pd nanoparticles. Likewise, bimetallic Pd/Pt nanoparticles were synthesized in porous carbon produced from biomass waste sorghum through a green CO_2-assisted route.[9] Although various green routes for the synthesis of Pd–Pt bimetallic nanoparticles exist, the RNA-mediated synthesis of such nanoparticles has not yet been reported. In this study, we, for the first time, report a one-pot green synthesis of bimetallic nanoparticles of Pd and Pt using RNA and ascorbic acid. First, Pd nanoparticles were formed, followed by the decoration of a Pt layer. The structural properties of the bimetallic nanoparticles were characterized using transmission electron microscopy (TEM), scanning transmission electron microscopy (STEM), energy-dispersive X-ray spectroscopy (EDX), and X-ray powder diffraction (XRD) methods. The catalytic properties of the nanoparticles were studied by the HER.

Fig. 1a and b shows the morphology of the synthesized bimetallic Pd–Pt(1) nanoparticles, where nanosponge-like particles of different sizes were formed. The polyionic structure of RNA might play an important role in controlling crystal growth and shape. The mean diameter of the nanoparticles was calculated to be 55 ± 13 nm. STEM analysis revealed the high-density particle core, which corresponds to the nanosponge morphology (Fig. 1c).[10] High-resolution TEM images show lattice planes of the crystals oriented in the (111) direction (Fig. 1d). XRD analysis of the particles revealed the presence of broad peaks of (111), (200), (220), and (311) diffraction planes (Fig. 1d). The broadness of the peaks could be attributed to the overlap of Pd and Pt diffraction planes.

[a] *Institute of Materials Science & Nanotechnology, UNAM-National Nanotechnology Research Center, Bilkent University, Cankaya, Ankara 06800, Turkey*
[b] *Department of Chemistry, Faculty of Science and Letters, Istanbul Technical University, Maslak, Istanbul 34469, Turkey. E-mail: topuzf@itu.edu.tr*
[c] *Fiber Science Program, Department of Human Centered Design, College of Human Ecology, Cornell University, Ithaca, NY 14853, USA. E-mail: tu46@cornell.edu*

† Electronic supplementary information (ESI) available: Morphology of Pt nanoparticles, cyclic voltammograms (CVs) of the nanoparticles and comparison of Pd–Pt nanocatalysts used for the HER. See DOI: https://doi.org/10.1039/d2ma01070d

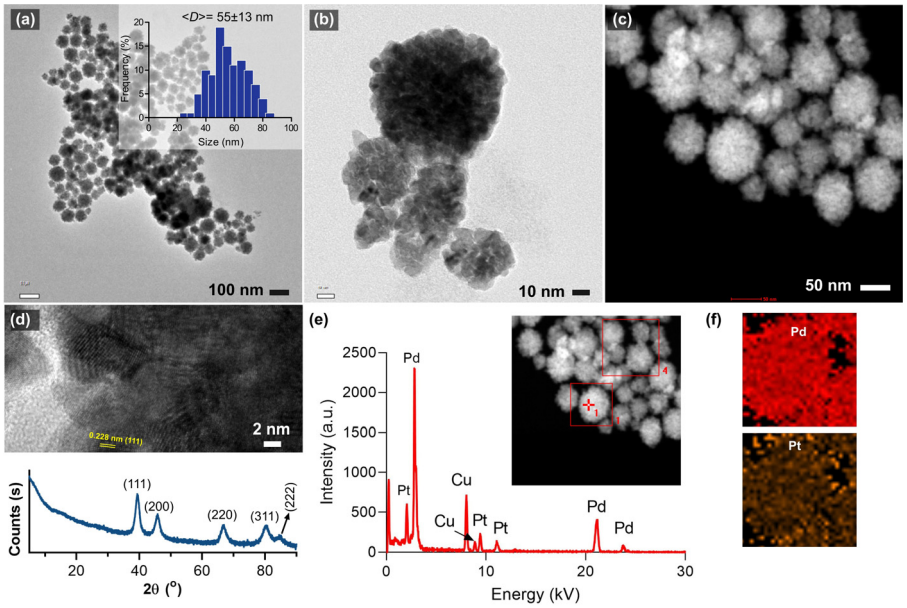

Fig. 1 Characterization of bimetallic Pd–Pt(1) nanosponges. (a and b) TEM images of Pd–Pt(1) nanosponges. The inset shows the size distribution of particles. (c) The STEM image of the nanosponges. (d) HRTEM image of the nanosponges showing the crystalline planes of the particles and the XRD pattern of the respective nanoparticles. (e) EDX analysis of the particles showing the presence of Pt and Pt and (f) the compositional elemental mapping of the bimetallic nanosponges.

A small peak at 84.6° assignable to the (222) plane was also observed. The EDX analysis of the nanosponges clearly shows their bimetallic structure. The atomic composition of Pd–Pt(1) was measured as 91.7% Pd and 8.3% Pt (Fig. 1e). Since the core Pd is formed first, it has a higher amount. The element mapping showed the homogeneous coating of the particles with a Pt layer (Fig. 1f). Fig. 2a shows the TEM images of the Pd–Pt(2) nanoparticles synthesized using a higher RNA content. Even though a similar morphology was observed for the nanoparticles, the resulting nanoparticles had denser domains as a result of a thicker Pt layer (Fig. 2b). This could be the result of nucleation/growth kinetics of the nanoparticles, which was manipulated by RNA molecules. The HRTEM analysis also showed the lattice planes of (111) for Pt (Fig. 2c). The SAED pattern of the Pd–Pt(2) nanoparticles confirmed their polycrystalline structure with corresponding diffraction rings of (111), (200), (220), and (311) planes (Fig. 2d). The STEM image of the nanosponges showed the formation of a denser core than the nanosponges fabricated at a lower RNA content (Fig. 2e). EDX analysis revealed the atomic composition of the Pd and Pt elements to be 89.1 and 10.9%, respectively, demonstrating the higher Pt content in the Pd–Pt(1) nanoparticles due to the

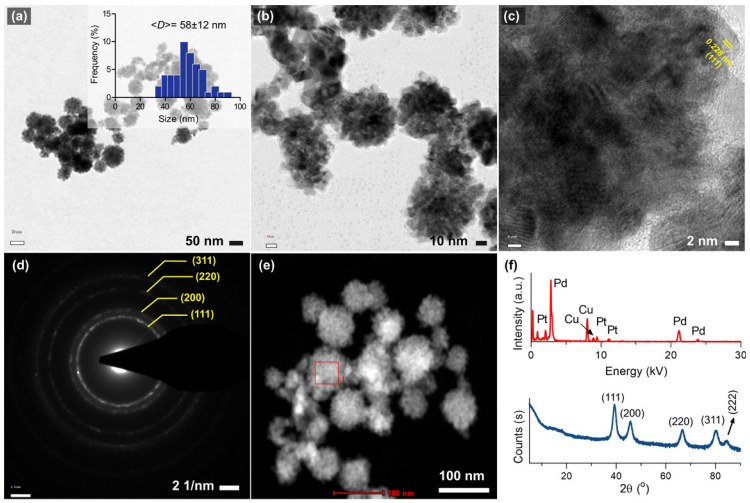

Fig. 2 Characterization of bimetallic Pd–Pt(2) nanosponges. (a and b) TEM images of Pd–Pt(2). The inset shows the size-distribution diagram of the respective nanoparticles. (c) A HRTEM image and (d) a SAED pattern of Pd–Pt(2) showing the crystalline planes of the particles. (e) The STEM image of Pd–Pt(2). (f) EDX analysis of the particles showing the presence of Pt and Pt and (f) XRD pattern of Pd–Pt(2).

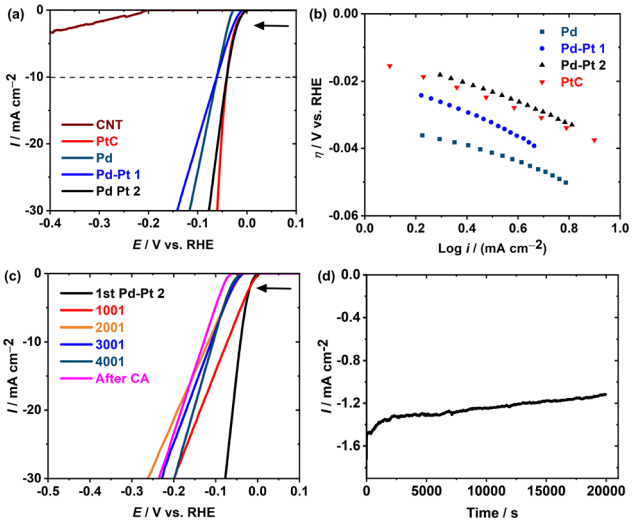

Fig. 3 (a) LSVs measured at the CNT, Pt/C, Pd, Pd–Pt(1), and Pd–Pt(2) with a sweep rate of 10 mV s^{-1} in 0.5 M H_2SO_4 and (b) Tafel plots (data used from Fig. 3a). (c) Polarization data in 0.5 M H_2SO_4 for Pd–Pt(2) initially and after 1000, 2000, 3000, and 4000 sweeps between +7.5 and −0.05 V *vs.* RHE at a scan rate of 100 mV s^{-1}. (d) Chronoamperometry at a constant potential at −0.05 V *vs.* RHE for 6 h (post-chronoamperometry LSV (*i.e.*, after CA) is shown in Fig. 3c).

presence of a thicker shell layer (Fig. 2f). The XRD pattern of the Pd–Pt(2) nanosponges showed the presence of (111), (200), (220), and (311) planes (Fig. 2f). The peak for the (222) lattice plane was clearer than that of the Pd–Pt(1) nanosponges. The bimetallic nanosponges (both Pd–Pt(1) and Pd–Pt(2)) were employed for the electrochemical HER. In this context, the linear sweep voltammograms (LSVs) recorded at the electrodes prepared with Pd, Pd : Pt (0.92 : 0.08), Pd : Pt (0.89 : 0.11), Pt/C, and multiwalled carbon nanotube modified glassy carbon electrodes are referred to as Pd, Pd–Pt(1), Pd–Pt(2), Pt/C, and CNT (Fig. 3). The results are summarized in Table 1 (the calculation details are elaborated in the Experimental section). Fig. 3a shows the anodic shift of *ca.* 26 mV in the HER onset potential (η) for Pd–Pt(2) compared to Pd, which is comparable with that of the state-of-the-art Pt/C. In addition, all of these catalysts showed higher HER catalytic activity than the bare CNTs, as expected. As per conventional comparison, η at 10 mA cm^{-2} (η_{10}) obtained at Pd–Pt(2) is 20 V anodic in comparison with Pd and Pd–Pt(1) proving the importance of the appropriate selection of the Pt/Pd ratio. The turnover frequency (TOF) value determined at an overpotential of 30 mV for Pd–Pt(2) is 0.0023 s^{-1} (Table 1), which is *ca.* 20 and 2 times higher than those of the Pd and Pd–Pt(1) nanoparticles, respectively, which is an additional proof of better HER catalysis. For miniature and low-weight devices, the mass activity (MA) estimated at Pd–Pt(2) is 7.63 mA g^{-1} which is *ca.* 17% better than that of Pt/C. The Tafel slopes demonstrate the HER mechanism at Pd, Pd–Pt(2), and Pt/C through the Volmer–Tafel pathway, whereas that at Pd–Pt(1) is through the Volmer–Heyrovsky pathway.[11] The stability of Pd–Pt(2) was analyzed over 4000 cycles of CV in the potential window of 7.5 to −0.05 V *vs.* RHE. Up to 4000 cycles after every 1000 cycles, LSVs are measured and referred to as 1001, 2001, 3001, and 4001 (Fig. 3c). After completing 4000 CV, chronoamperometry at −0.05 V *vs.* RHE for 6 h (Fig. 3d) was performed on the same electrode.

A long-duration cyclic and chromatographic stability at Pd-Pt(2) shows a slight cathodic potential shift in the η and η_{10} (*i.e.*, 55 mV and 85 mV, respectively). The stable response of Pd–Pt(2) is proposed to be an effect of the strains and ligands induced between Pd and Pt interactions having similar lattice constants, which are in line with the diffraction pattern (Fig. 2f). These results indicate that the influence of the different ratios of Pt and Pd can strongly influence the HER kinetics and mechanism. Furthermore, with a 10-fold less amount of pure Pt (in Pd–Pt(2)), a similar electrochemical efficiency to Pt/C is achieved at Pd–Pt(2) with increased MA (than Pt/C).

Conclusions

A green one-pot synthesis of bimetallic nanoparticles of Pd and Pt using RNA and ascorbic acid was, for the first time, reported. The thickness of the shell layer could be tuned with the RNA content. The nanosponge particles with a mean size in the range of 55–58 nm could be synthesized. EDX analysis confirmed the bimetallic core–shell structure of Pd and Pt. The HRTEM, SAED, and XRD analyses revealed the polycrystalline structure of the particles. Bimetallic nanoparticles showed high performance in the HER by tuning the composition of the nanoparticles. Overall, this study demonstrates the ease of tuning the ratio of Pd and Pt in bimetallic nanoparticles, with a 10-fold lower amount of Pt (in Pd–Pt2) than that in pure Pt/C showing equivalent catalytic activity to the state-of-the-art Pt/C with improved stability and mass activity towards the HER.

Experimental section

Materials

Palladium(II) acetate ($(Pd(OAc)_2)$, Pd: 45.9–48.4%) and sodium tetrachloroplatinate ($Na_2PtCl_4{\cdot}xH_2O$, Pt: 42.67%) were

Table 1 Summary of electrocatalytic results

	ECSA/ cm^2	RF	η/mV	η_{10}/mV	Tafel slope/ $mVdec^{-1}$	j_g @ η = 0.030 V/ $mAcm^{-2}$	j_s/mA cm^{-2}	TOF @ η = 0.030 V/s^{-1}	i_0/ $mAcm^{-2}$	MA/ mAg^{-1}
CNT	—	—	−200	—	—	—	—	—	—	—
Pd	15.341	217.06	−28.5	−60	25	−0.33	−0.002	0.00013	1.07	0.47
Pd–Pt(1)	10.384	146.93	−11.2	−61	39	−2.71	−0.018	0.00113	1.04	3.83
Pd–Pt(2)	10.434	147.63	−2.0	−40	29	−5.41	−0.036	0.00229	1.02	7.63
Pt/C	2.03	28.63	−3.0	−41.5	28	−4.50	−0.157	0.00321	1.03	6.33

purchased from Alfa Aesar (Germany). L-Ascorbic acid (AA, Sigma-Aldrich) and ribonucleic acid sodium salt (RNA from yeast, TCI Chemicals) were used as received. 20% Platinum on graphitized carbon (<5 nm (Pt); Pt/C) was purchased from Sigma-Aldrich.

Synthesis of Pd–Pt bimetallic nanoparticles

RNA (5 mg for Pd–Pt(1) or 10 mg for Pd–Pt(2)) was dissolved in water and heated to 80 °C, after which ascorbic acid (50 mg) was added, and the solution was stirred until complete dissolution. Thereafter, an aqueous solution of $Pd(OAc)_2$ (100 mg in 5 mL of water) was added dropwise and the mixture was stirred for 60 min. Thereafter, the mixture was treated with Na_2PtCl_4 (50 mg in 5 ml water) and stirred for further 120 min. Pd nanoparticles were synthesized following the same procedure for mixing at 3 h without the addition of Na_2PtCl_4.

To prove the formation of nanosponge shaped particles with RNA, Pt nanoparticles were also prepared using RNA/ascorbic acid in the absence of Pd precursor *via* the same route. The morphology of the resulting nanoparticles is shown in Fig. S1 and S2 (ESI†).

Characterization

TEM images were obtained on a Tecnai G2F30 (FEI) instrument. The nanoparticles were dispersed in water and dried on a carbon-coated grid. TEM was operated with an acceleration voltage of 300 kV. High-angle annular dark-field (HAADF) imaging in a scanning transmission electron microscope (STEM) was used to characterize the nanoparticles. XRD experiments were performed using a PANalytical X'Pert Pro MPD powered by a Philips PW3040/60 X-ray generator equipped with an X'Celerator detector. Diffraction data were obtained by exposing the samples to Cu-K X-rays. X-rays were generated from a Cu anode powered at 40 kV and a current of 40 mA. The data were analyzed with the software X'Pert HighScore Plus (version 2.0).

HER experiments

All experiments were performed at room temperature using a Biologic SP-150 potentiostat with a standard three-electrode electrochemical cell. The catalyst-modified glassy carbon electrode (GC, 3 mm diameter, 0.07068 cm^2 of geometric surface area), Pt spiral wire, and $Ag|AgCl|KCl_{(sat.)}$ were used as the working, counter, and reference electrodes, respectively. The HER studies were performed in an acidic medium, *i.e.*, 0.5 M H_2SO_4. The Nernst equation (SE1) is used to convert all the potentials measured *vs.* $Ag|AgCl|KCl_{(sat.)}$ to the reversible hydrogen electrode (RHE):[12]

$$E_{RHE} = E_{Ag|AgCl|KCl(sat.)} + 0.059\ pH + E^{\circ}_{Ag|AgCl|KCl(sat.)} \quad (1)$$

where E_{RHE} is the potential estimated *vs.* RHE, $E_{Ag|AgCl|KCl(sat.)}$ is the measured potential *vs.* the $Ag|AgCl|KCl_{(sat.)}$ electrode, and $E^{\circ}_{Ag|AgCl|KCl(sat.)}$ is the standard electrochemical potential of the $Ag|AgCl|KCl_{(sat.)}$ electrode, *i.e.*, 0.197 V.

The electrocatalyst slurries were prepared by mixing 8 mg catalyst (Pd, Pd–Pt(1), Pd–Pt(2), and Pt/C) and 16 mg multi-walled carbon nanotubes (MWCNTs) in 500 μL of DI water, 100 μL of ethanol, and 40 μL of 5 wt% Nafion solution, followed by vortexing for 10 min. The GC surface was cleaned with aqueous slurries of alumina powder (first with 1 μm and later 0.06 μm) with the help of a polishing micro cloth. To remove the alumina, the electrode was ultrasonically cleaned with 18 MΩ Millipore water and then with ethanol for 10 min, individually. To fabricate Pd, Pd–Pt(1), Pd–Pt(2), and Pt/C modified GC electrodes, 4 μL electrocatalyst slurry was drop-casted on the cleaned GC electrodes individually. Thus the prepared electrodes were dried in an oven at 60 °C for 30 min before electrochemical measurements. All the calculations were performed based on the geometric surface area unless specified otherwise.

Calculations

The specific current densities (j_s) corresponding to j_g were calculated using eqn (2):

$$j_s = j_g/RF \quad (2)$$

The rate of electrons delivered per surface metal atom per second or the rate of product molecules evolved per surface metal atom was determined from turnover frequency (TOF) based on eqn (3):[13]

$$TOF = I/(4 \times F \times m) \quad (3)$$

where I is the measured current in amperes, F is the Faraday constant and m is the number of moles of the active catalyst. Moles were estimated based on the ratio of Pd and Pt (the ratio of Pt to Pd was determined from the EDX atomic percentage) and the molar mass of their respective elements. It was assumed that all of the materials in the catalysts are catalytically active for the HER.

The mass activity was estimated as j_g/total mass of the catalyst (g).

The electrochemical active surface area (ECSA) was estimated from the reduction of a monolayer of PdO and the UPD of the hydrogen region from the CV (Fig. S3, ESI†) by considering 420 μC cm^{-2} [14,15] and 210 μC cm^{-2} [15,16] as the standard unit charges for Pd and Pt per square centimeter, respectively. The charge under the monolayer of the UPD hydrogen region at Pd and Pt was fragmented based on the atomic weight percentage measured by EDX. Although the roughness factor differs based on the facet orientations in the catalyst, to estimate the roughness factor we have considered and estimated it based on the conventional standards. The roughness factor (RF) was calculated by dividing ECSA by the geometric surface area.[13]

Author contributions

F. T. and T. U. conceived the project. F. T., B. P., and T. U. wrote the draft of the manuscript. F. T. synthesized and characterized the nanoparticles. B. P. performed the electrochemical measurements.

The manuscript was written through the contributions of all authors. All authors approved the final version of the manuscript.

Conflicts of interest

The authors declare no competing financial interest.

Notes and references

1 S. Anwar, F. Khan, Y. Zhang and A. Djire, *Int. J. Hydrogen Energy*, 2021, **46**, 32284–32317.
2 Z. Wei, J. Sun, Y. Li, A. K. Datye and Y. Wang, *Chem. Soc. Rev.*, 2012, **41**, 7994–8008.
3 S. Hu, G. Goenaga, C. Melton, T. A. Zawodzinski and D. Mukherjee, *Appl. Catal., B*, 2016, **182**, 286–296.
4 B.-W. Zhang, H.-L. Yang, Y.-X. Wang, S.-X. Dou and H.-K. Liu, *Adv. Energy Mater.*, 2018, **8**, 1703597.
5 M. F. Lengke, M. E. Fleet and G. Southam, *Langmuir*, 2007, **23**, 8982–8987.
6 F. Gulbagca, A. Aygün, M. Gülcan, S. Ozdemir, S. Gonca and F. Şen, *Appl. Organomet. Chem.*, 2021, **35**, e6272.
7 F. Topuz and T. Uyar, *J. Colloid Interface Sci.*, 2019, **544**, 206–216.
8 D. Liu, L. A. Gugliotti, T. Wu, M. Dolska, A. G. Tkachenko, M. K. Shipton, B. E. Eaton and D. L. Feldheim, *Langmuir*, 2006, **22**, 5862–5866.
9 D. Hu, H. Xu, Z. Yi, Z. Chen, C. Ye, Z. Wu, H. F. Garces and K. Yan, *ACS Sustainable Chem. Eng.*, 2019, **7**, 15339–15345.
10 Z.-H. Lin, M.-H. Lin and H.-T. Chang, *Chem. – Eur. J.*, 2009, **15**, 4656–4662.
11 B. Patil, B. Satilmis, M. A. Khalily and T. Uyar, *ChemSusChem*, 2019, **12**, 1469–1477.
12 R. Mishra, B. Patil, F. Karadaş and E. Yılmaz, *ChemistrySelect*, 2017, **2**, 8296–8300.
13 T. G. Ulusoy Ghobadi, B. Patil, F. Karadas, A. K. Okyay and E. Yilmaz, *ACS Omega*, 2017, **2**, 8319–8329.
14 L. Fang, Q. Tao, M. Li, L. Liao, D. Chen and Y. Chen, *Chin. J. Chem. Phys.*, 2010, **23**, 543–548.
15 M. Shao, J. H. Odell, S.-I. Choi and Y. Xia, *Electrochem. Commun.*, 2013, **31**, 46–48.
16 C. P. Andrieux and J. M. Savéant, *J. Electroanal. Chem. Interfacial Electrochem.*, 1970, **28**, 446–450.